



university of  
 groningen

kvi - center for advanced  
 radiation technology

# PET geometries and protocols for verification of Proton therapy

evaluation of PET images

Bachelor thesis

July 2016

Student: R.B. Hijlkema

Primary supervisor: Dr. P.G. Dendooven

Secondary supervisor: Dr. K.W. Brzezinski

RUBEN HIJLKEMA

This work was performed in the Medical Physics Group of KVI-Center for Advanced Radiation Technology, University of Groningen. This Bachelor Research Project was performed as part of the BSc Physics degree programme of the Faculty of Mathematics and Natural Sciences, University of Groningen.



## ABSTRACT

---

In proton therapy, the dose deposition reaches a maximum at the end of the trajectory known as the 'Bragg Peak'. This leads to a higher precision of dose-delivery while simultaneously a clinical error in the treatment could lead to a high dose in healthy tissue. A method of verifying whether the intended dose was accurately delivered to the patient is desired. Imaging the positron emitting nuclides that are produced by the proton beam in the patient, using positron emission tomography (PET) is currently a promising method being studied in several treatment centers. In this thesis, emission-map images of a head-and-neck patient are evaluated using the  $\gamma$ -index and the SSIM-index. For an *in-beam* dual-head PET-scanner and an *in-room* full-ring PET-scanner simulated through *Monte-Carlo Simulations*.



## ACKNOWLEDGMENTS

---

Many thanks to Karol Brzezinski, my daily supervisor, for clear insight and understanding of the material. Also thanks to Bas van der Zee who had a big part in this collaborative project, especially for running the simulations. Thanks to Peter Dendooven for various insights and structure of this thesis.



# CONTENTS

---

1	INTRODUCTION	3
1.1	Proton Therapy	5
1.1.1	Interaction	5
1.1.2	Positron Emission Tomography	6
2	METHODS	9
2.1	Treatment Plan	9
2.2	Protocols	9
2.2.1	Protocol 1: in-room PET	10
2.2.2	Protocol 2: in-beam PET	10
2.2.3	Protocol 3: in-beam PET	10
2.3	Emission-map acquisition	10
2.3.1	Data Adjustments	14
2.4	Image Comparison	14
2.4.1	The gamma-index	15
2.4.2	The SSIM-index	16
3	RESULTS	19
3.1	Discussion	20
4	CONCLUSIONS	25
	BIBLIOGRAPHY	27

## LIST OF FIGURES

---

Figure 1	The dose deposition curve of protons	6
Figure 2	Nuclide activity with a proton energy deposition curve	7
Figure 3	Transverse view of the patient, with lines indicating the direction of the incoming treatment beam for each of the 5 fields	9
Figure 4	Visualization of the time structure of the scanning protocols	11
Figure 5	Scanner positioning	12
Figure 6	3D representation of the detectors	13
Figure 7	A schematic representation of the $\gamma$ -index	17
Figure 8	PCC score of the three protocols over different iterations of image reconstruction	20
Figure 9	Transverse slices of the patient with different reconstructed images of different protocols taken halfway through the transverse orientation.	21
Figure 10	Sagittal slices of the patient with different reconstructed images of different protocols taken halfway through the sagittal orientation	22

## LIST OF TABLES

---

Table 1	Nuclear reaction channels	7
Table 2	Treatment plan fields	10
Table 3	Scanner specifications	13
Table 4	Number of Coincidences per protocol	19
Table 5	Scores of different image comparison methods	23

## ACRONYMS

---

PET	positron emission tomography
ToF	time of flight
MLP	most likely position
DTA	distance to agreement
LoR	line of response

SSIM structural similarity-Index

PCC Pearson correlation coefficient

ML-EM maximum likelihood - expectation maximization

HVS human Visual system

CTW coincidence timing window







## INTRODUCTION

---

Proton therapy uses protons to deliver the dose to a patient's tumor, instead of photons. The main advantage of using protons, over photons, as used in conventional radiotherapy is the highly specified dose distribution at the end of a proton trajectory with the abrupt fall-off, the so called '*Bragg Peak*'. This allows for a high-precision dose delivery to the tumor, while sparing surrounding critical organs. However, uncertainties in the delivery of the dose distribution can lead to a high dose in surrounding tissue. The treatment planning process is highly susceptible to uncertainties that arise from CT artifacts, CT resolution and the conversion of CT data to Hounsfield-Units[1][2]. Furthermore, uncertainties arise from the actual treatment, including positioning errors, organ movement[3] and anatomical changes such as tumor shrinkage[4] and patient weight changes. Therefore, a method to verify the intended dose delivery is desired.

Protons going through tissue create a small fraction of positron emitting isotopes. The  $\beta^+$ -decay of these isotopes, followed by the positron's annihilation with an electron from the surrounding tissue, leads to two back-to-back annihilation photons which can be detected by positron emission tomography (PET), providing a method to verify the delivered dose distribution with respect to the treatment plan.

The acquisition of these dose distribution images is not trivial. The positron emitting isotopes that are produced as a result of the proton beam interacting with tissue are short-lived. To achieve the best result possible, it is of the utmost importance that the time between the treatment and the verification be as short as possible. To this end, there are three general PET scanning protocols [5]:

1. *in-beam*: A dedicated PET scanner is integrated into the beam delivery system. The scanning can start immediately after the treatment or in-between fields. The advantage is that the activities of the isotopes produced are highest with in-beam PET scanning. However, when implementing the in-beam method geometry is a limitation. The scanner must leave room for the beam delivery system and needs to be flexible enough for patient positioning. Therefore, the most common in-beam scanning system is the *dual-head* configuration[6][7].
2. *in-room*: The PET scanner is located in the same room as the beam delivery system and scanning can start after the whole treatment plan with a short delay. The advantage is the full angular coverage of a full-ring PET scanner at the cost of a lower isotope activity.
3. *off-line*: The PET scanner is not located nearby the beam delivery system and the scanning has a significant delay, resulting in a

lower isotope activity. The advantage is that any PET scanner located in the hospital can be used for this method.

The goal of this research is to compare reconstructed emission-map images, simulated by *Monte-Carlo Simulations*, of a *dual-head in-beam* scanner and a *full-ring in-room* scanner for different protocols. To find an optimal procedure for PET-verification of proton therapy.

## 1.1 PROTON THERAPY

Proton therapy is an interesting option for patient treatment due to the physics of the irradiation method. The dose deposition per unit length of protons is the highest at the end of the trajectory, the so-called '*Bragg Peak*'. The dose deposition per unit length of photons takes on the form of an exponential decay with a maximum at the beginning of the trajectory. Subsequently, for photons to deposit a sufficient amount of dose in the tumor, the tissue behind the tumor is irradiated too, since the photons do not stop in the tumor. Proton therapy allows for a precise delivery of dose while sparing critical tissue surrounding the tumor, due to the characteristic form of the dose-deposition curve of protons.

### 1.1.1 Interaction

#### 1.1.1.1 Stopping Power

A heavy charged particle loses its energy by inelastic collisions causing ionization and excitation of atoms. The amount of energy lost per unit length is called the *stopping power*. The stopping power can be described with the Bethe-Bloch equation [8]:

$$-\frac{dE}{dx} = \frac{4\pi\epsilon_0^2 z^2 N}{mv^2} Z \left( \log \frac{2mv^2}{I} - \log(1 - \beta^2) - \beta^2 \right) \quad (1)$$

where  $c$  is the speed of light and  $\epsilon_0$  the vacuum permittivity,  $\beta = v/c$  with  $v$  the velocity of the particle,  $I$  the mean ionizing potential,  $z$  the atomic number of the incident particle,  $Z$  the atomic number of the target material,  $N$  Avogadro's number,  $e$  and  $m$  the electron charge and rest mass respectively.

From equation 1 it is seen that at higher proton velocities, less energy is deposited per unit length. From this the energy deposition curve takes on its characteristic form, gradually losing energy before coming to a quick stop, as most energy is deposited at low velocities as seen in figure 1.

#### 1.1.1.2 Nuclide fragmentation

Protons traversing tissue cause target fragmentation. Target fragmentation is the process of creating excited pre-fragments and photon emission by means of ablation of the target nuclei [9]. Protons cannot produce positron-emitting projectile fragments since their atomic mass is too low. Through target fragmentation, nuclei are produced that undergo  $\beta^+$ -decay. The reaction products that are formed in tissue are given in table 1. These fragments are formed along the proton beam path, as long as the energy of the protons is sufficient to induce nuclear reactions. This corresponds to a threshold energy of 10 – 20 MeV. These energies occur about 1-4 mm before the Bragg peak as seen in figure 2.

The nuclides produced stay close to their place of production, allowing for a direct correspondence of the beam path and the activity

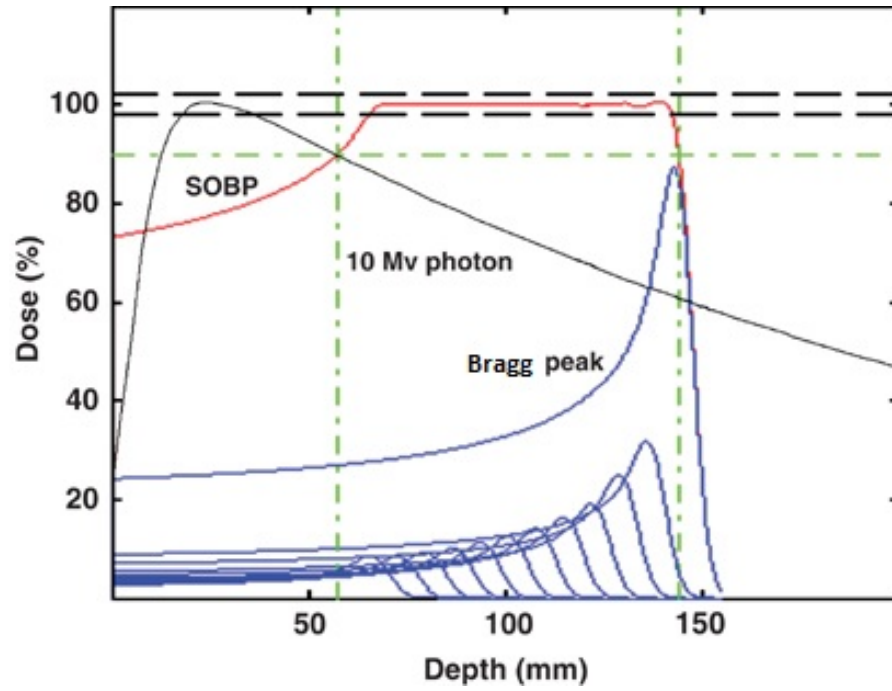
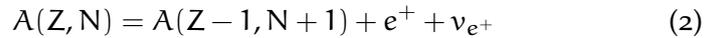


Figure 1: The dose deposition curve of protons, in blue, and photons, in black. The red line depicts the spread out Bragg Peak (SOBP).

of the nuclides. These nuclides are  $\beta^+$ -emitters, meaning that the decay takes on the form of:



A proton changes to a neutron and a neutrino and subsequently a positron is emitted. The mean distance traveled by the positron from the site of production is around 1 mm [10]. It comes to rest due to inelastic collisions with the patient's tissue. When at rest, the positron combines with an electron and two 511 keV annihilation photons are created, which, according to conservation of momentum, have to be emitted back-to-back. These back-to-back photons are the underlying physics of PET. The nuclides that are clinically most relevant are  $^{15}\text{O}$ ,  $^{11}\text{C}$  and  $^{13}\text{N}$  due to their half-life and activity. The activity of  $^{15}\text{O}$  is the highest right after treatment, but diminishes quickly and  $^{11}\text{C}$  becomes the dominant determined [5]. Therefore, it is of importance that scanning is done as quickly as possible after the treatment.

### 1.1.2 Positron Emission Tomography

PET uses the fact that  $\beta^+$  emitters produce two back-to-back photons with an energy of 511 keV. By measuring these photons in coincidence, a line of response (LoR) can be determined. When combined with timing information, time of flight (ToF)-PET, may help in determining the position of annihilation on the line of response. Photons can interact with matter in three different ways;

1. *the photo-electric effect*: The energy of the photon is used to eject an electron out of the electron-shell of an atom. The photon is absorbed in this process.

Table 1: Nuclear reaction channels

Produced nuclide	Half life (s)	Reaction channel	Threshold energy (MeV)
$^{15}\text{O}$	122.24	$^{16}\text{O}(\text{p},\text{pn})^{15}\text{O}$	16.79
$^{11}\text{C}$	1220.04	$^{12}\text{C}(\text{p},\text{pn})^{11}\text{C}$	20.61
		$^{14}\text{N}(\text{p},\alpha)^{11}\text{C}$	3.22
		$^{16}\text{O}(\text{p},\alpha\&\text{pn})^{11}\text{C}$	59.64
$^{13}\text{N}$	597.9	$^{14}\text{N}(\text{p},\text{pn})^{13}\text{N}$	11.44
		$^{16}\text{O}(\text{p},\alpha)^{13}\text{N}$	5.66
$^{14}\text{O}$			
$^{10}\text{C}$			
$^{30}\text{P}$	149.88	$^{31}\text{P}(\text{p},\text{pn})^{30}\text{P}$	19.7
$^{38}\text{K}$	458.16	$^{40}\text{Ca}(\text{p},\alpha)^{38}\text{K}$	21.2

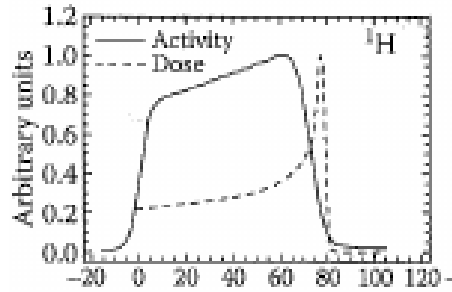


Figure 2: Nuclide activity with a proton energy deposition curve. The nuclides are produced at a certain threshold energy which corresponds to a fall-off of activity before the Bragg Peak

2. *Compton scattering*: The inelastic scattering of a photon by a charged particle (an electron in this case). The scattered photon has less energy than the incident photon, as per conservation of energy and momentum.
3. *pair production*: The incident photon interacts with a heavy nucleus to form a positron-electron pair. The energy needed for this reaction to occur has to be at least the rest-mass of the positron-electron pair, i.e.  $2 \cdot 511\text{keV}$

The type of interaction is dictated by the energy of the incident photon and the effective atomic number of the material. With body tissue having an effective atomic number between  $Z_{\text{eff}} = 4 - 10$  [11] and the  $\beta^+$ -emitters always producing two 511 keV photons, it follows that Compton scattering is the dominant process.

ToF-PET measures coincidence photons with a timing resolution, meaning that two back-to-back photons that are detected on opposite detectors within a certain timing window are counted as coincidences. ToF-PET improves on normal PET by using this timing information to determine a most likely position (MLP) on the LoR. Timing resolutions are down to 325ps on state of the art scanners (Phillips,2015)[12].

Based on the photon interactions and the finite timing resolution of PET, there can occur three types of coincidences. A true coincidence occurs when two back-to-back photons are measured within the coincidence timing window (CTW) in detectors on opposite sides of the location of the annihilation event. A random coincidence is detected when two photons are measured on opposite detectors that don't originate from the same annihilation event. Lastly, a scattered coincidence occurs when two back-to-back photons are measured in coincidence and at least one photon had scattered. The random and scattered coincidences both result in a mismatch between the assigned LoR and the actual LoR. These errors can be partially resolved by using correction methods for random- and scattered coincidences [13] and the detector's energy resolution, since the scattered photons do not have the same energies as non-scattered photons.

For the best results it is of importance to get as many coincidences as possible. To achieve the highest number of coincidences, a high activity of  $\beta^+$ -emitters is desired. With half-lives as short as 2 minutes, as seen in table 1, it is of importance to scan as soon as possible after treatment.

## METHODS

### 2.1 TREATMENT PLAN

The emission-maps are simulated based on the treatment plan of a patient with a tumor in the neck, a so called *head-and-neck case*, as seen in figure 5. Dual-head PET verification is especially beneficial for a head-and-neck case, since the smaller dimensions of the head lead to a more flexible positioning of the dual-head panels. Moreover, the distance between the panels can be smaller compared to e.g. a breast case, allowing for a higher resolution and sensitivity in the tumor.

The patient was treated with 5 fields, each field directed from a different angle as to spare surrounding healthy tissue, as seen in figure 3. The order of the fields is taken from the treatment plan. The angles of irradiation are given in table 2(a) along with the order and time of irradiation of each field. The rotation time in-between fields is given in table 2(b).

### 2.2 PROTOCOLS

Three different protocols were established, two in-beam PET protocols with a dual head scanner and an in-room PET protocol with a full-ring scanner.

The total scanning time is taken at a constant of 2 minutes, to reduce the impact of PET verification on patient-throughput and to eliminate scanning time as a factor in the comparison between the protocols. The rotation speed of the gantry is 1 revolution per minute [14]. A delay of 60 seconds from treatment to scanning for *in-room*

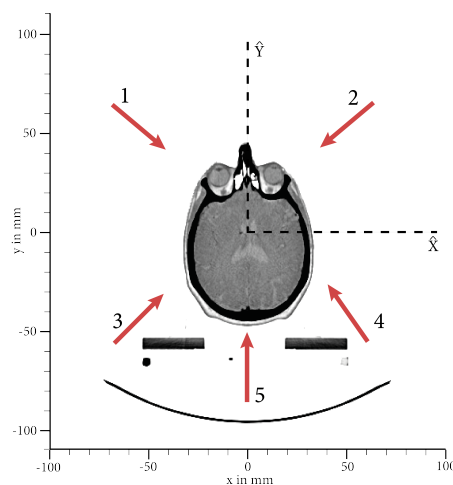


Figure 3: Transverse view of the patient, with lines indicating the direction of the incoming treatment beam for each of the 5 fields

Table 2: Treatment plan fields. Note: five seconds of delay are added to each rotation to account for overhead of the gantry rotation

Field	Angle (deg)	Time (s)	Rotation	Angle (deg)	Time (s)
1	310	75.6	1	100	21.6
2	50	75.0	2	175	34.2
3	225	84.0	3	80	18.3
4	145	72.8	4	35	10.8
5	180	82.5	5	50	13.3

(a) (b)

scanning is taken as a realistic value. A description of each protocol is given below together with a visual representation in figure 4, taking into account treatment times, rotation times, scanning times and decay times.

### 2.2.1 Protocol 1: in-room PET

The patient is treated according to the treatment plan and afterwards scanned with a full-ring scanner. The delay between treatment and scanning is set to 60 seconds. The scan has a duration of 2 minutes.

### 2.2.2 Protocol 2: in-beam PET

The patient is scanned for 60 seconds after field 1 and for 60 seconds after the field 5, in both cases the dual-head panels are placed parallel to the beam direction as can be seen in figure 5c and figure 5d. Should there be errors in beam-delivery, a scan in-between fields allow for adjustments of beam-delivery for subsequent fields.

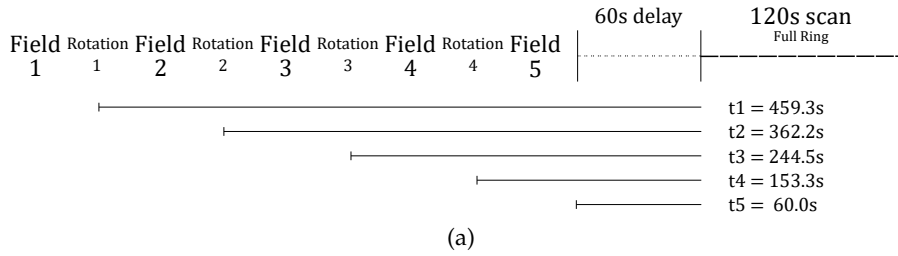
### 2.2.3 Protocol 3: in-beam PET

The patient is scanned for 2 minutes after the treatment with a change of panel position halfway through. The panels start out parallel to the beam direction of field 5, as can be seen in figure 5c. The nature of the exponential decay of the isotopes requires that the last treated field must be scanned first, as to receive optimal statistics. Furthermore, starting in this position removes unnecessary rotation times. After 60 seconds the dual-head panels are rotated parallel to the direction of field 1, as can be seen in figure 5d, and a scan of 60 seconds is performed.

## 2.3 EMISSION-MAP ACQUISITION

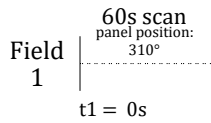
The emission maps are simulated based on the treatment plan of the patient. First a positron emitting isotope map is simulated with *Monte-*

### Protocol 1

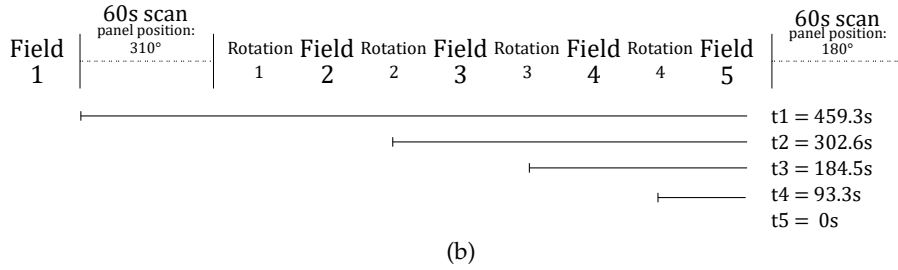


### Protocol 2

#### Protocol 2A

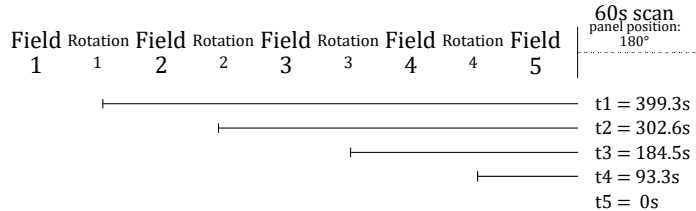


#### Protocol 2B



### Protocol 3

#### Protocol 3A



#### Protocol 3B

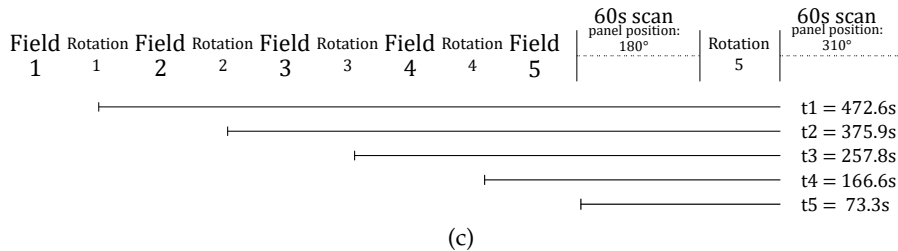


Figure 4: Visualization of the time structure of the scanning protocols. (a) Protocol 1, scanning with a full ring scanner after the treatment containing a delay of 60s between treatment and scanning. (b) Protocol 2, scanning with a dual head scanner after field 1 and field 5. Note that the protocol is divided in two as to contain the time structure for the simulation. (c) Protocol 3, two scans with the dual-head scanner 60 seconds after the treatment.

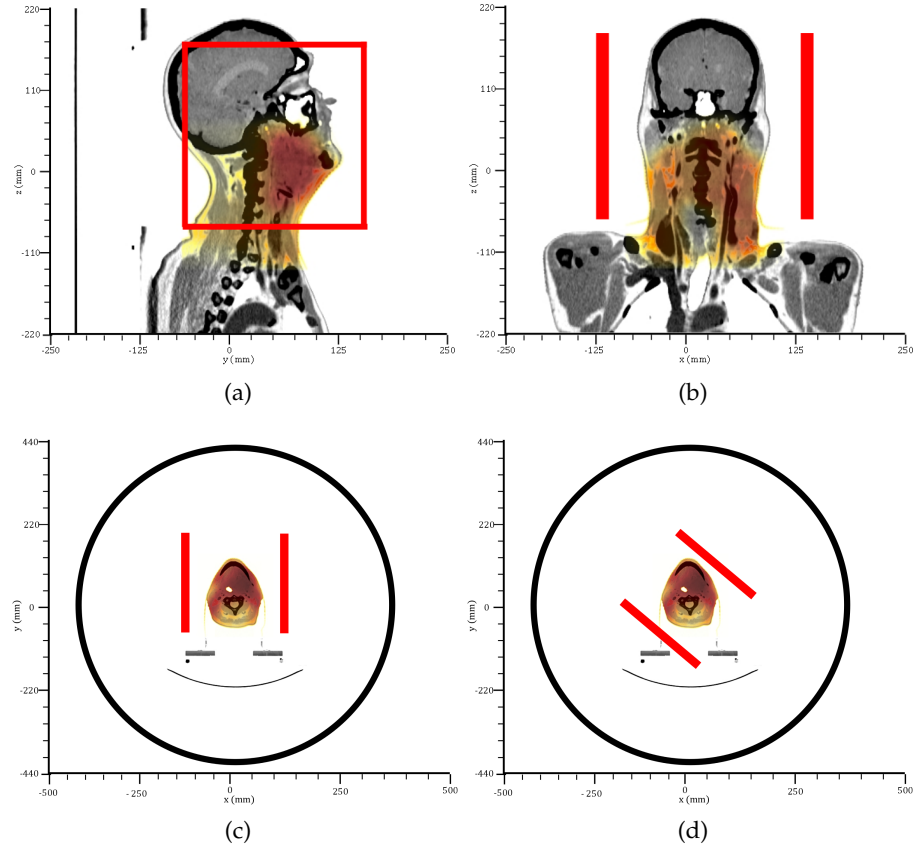


Figure 5: Scanner positioning. (a) and (b) the production map abundance in the patient, overlaid with the patient's CT, with an outline of the dual-head scanner represented in red, positioned parallel to beam 5, for the sagittal and coronal view respectively. (c) Transverse view of the patient with a schematic representation of full-ring PET in black. In red the dual-head scanners positioned to measure field 5, with a distance of 320 mm in (c), and in (d) positioned to measure field 1, with a distance of 350 mm.

*Carlo* using *Geant4* based on the 5 fields given in the treatment plan. From these isotope maps a second simulation was done. Simulating the positron emission and PET detection from within the phantom by means of *Monte Carlo simulation* using *Gate*. These simulations consist of three main components;

1. *the PET scanner*: there are two different scanners depending on the PET protocol. The full-ring detector is used in *in-room* protocols, the dual-head detector is used in *in-beam* protocols. The characteristics of the detectors can be seen in table 3 and a visual representation of both scanners can be seen in figure 6.
2. *the production map*: The production map contains the location and abundance of the nuclides. Each nuclide has its own distribution which can be used separately in *Gate* allowing for separate decay constants. The production maps are adjusted for decay constants in order to create activity distributions and then loaded into the simulation.

3. *the phantom*: A phantom is the object which contains the attenuation material. In the simulations, a phantom is used based on the CT image of the patient. The original CT-scan has a size of  $500 \times 500 \times 410$  pixels, where each voxel has a volume of  $1 \times 1 \times 1 \text{ mm}^3$ . the CT-scan contains Hounsfield Units, with a minimum of -1024. To write the CT-scan in unsigned integer, a value of 1024 has been added to each voxel, this has been corrected for in *Gate*. To be able to place the dual-head panels as close as possible to the patient's head the CT-scan has to be cropped. Due to the phantom containing air and limitations of *Gate* not allowing the detectors to be placed inside the phantom the CT-scan is cropped to a size of  $200 \times 250 \times 410$  pixels, to allow for detector placement.

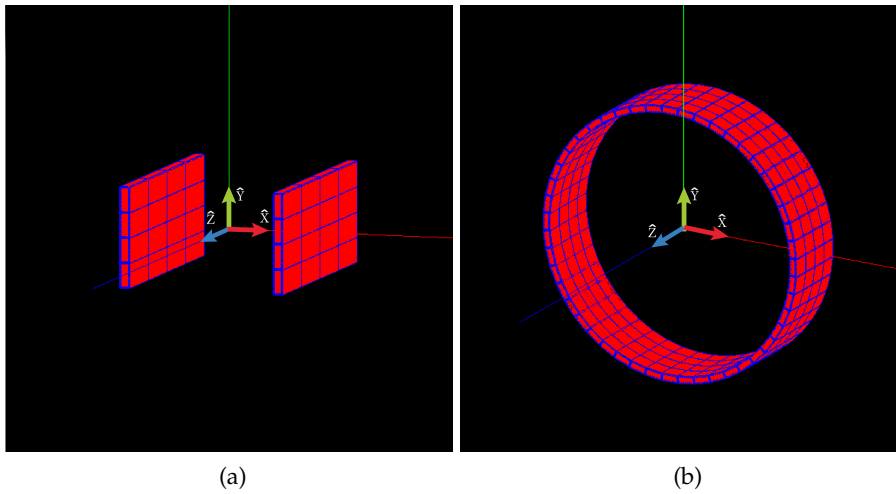


Figure 6: 3D representation of the detectors. (a) The dual-head panels. (b) The full ring detector.

Table 3: Scanner specifications. Note: dual-head contains two different diameters, due to the dimensions of the head the detectors can be placed closer together when scanning field 5.

	Full-ring	Dual head
diameter (mm)	842	350 (field 1) 320 (field 5)
Axial FOV (mm)	218.4	218.4
Number of Blocks	192	2 x 16
Number of Crystals per block	169	169
Dimensions Block (x, y, z)	20, 54.6, 54.6	20, 54.6, 54.6
Dimensions Crystal (x, y, z)	20, 4, 4	20, 4, 4
Scintillation Material	LSO	LSO

### 2.3.1 Data Adjustments

The production maps were adjusted for the simulations to convert to activity values and to contain the time structure. The nuclide activity map used in *Gate* is given by;

$$\text{Nuclide activity map} = \text{Production map} \times \lambda e^{(-\lambda t)} \times 285 \quad (3)$$

In the simulation of the treatment, one out of every 285 protons was simulated. A multiplication with  $\lambda$  is done to convert from the number of nuclides per voxel to activities.  $\lambda$  is calculated as;

$$\lambda = \frac{\ln(2)}{t_{\frac{1}{2}}} \quad (4)$$

The nuclide activity map has also been multiplied with a decay factor to include the timing structure  $e^{-\lambda t}$ . Where  $\lambda$  is the respective decay rate of the nuclide and  $t$  the time passed between treatment and scanning as seen in figure 4. Furthermore, the nuclide map is written in float and *Gate* requires the data to be written in unsigned integers, 16 BIT. The factors mentioned above result in voxel values of the order of 1. Unsigned integer 16 BIT has a range of 0 through 65,535 ( $2^{16} - 1$ ). To retain precision in the writing of the data, the nuclide map has been multiplied with a factor of  $10^4$ , taking advantage of the range of unsigned 16 BIT integers. This factor has been taken into account in *Gate* where these values are brought down to their original values by a division of the activity by  $10^4$ .

## 2.4 IMAGE COMPARISON

The *Gate* output was reconstructed using the maximum likelihood - expectation maximization (ML-EM) algorithm including correction for attenuation. Random coincidence correction was not performed due to low activity. Scattered events were not used in the reconstruction. The reconstructed images were compared to the emission map. The emission map is the nuclide activity map corrected for the decay during scanning, i.e.:

$$\text{Emission map} = \text{Nuclide activity map} \times (1 - e^{-\lambda t_{scan}}) \quad (5)$$

where  $t_{scan}$  is the scan duration. Given sufficient statistics, increased iterations of the ML-EM algorithm converges to the most likely activity distribution in the phantom. However, since statistics are limited, by increasing iteration the statistical noise gets amplified and therefore one expects a maximum of image fidelity at a certain iteration number. This maximum has been found by calculating the Pearson correlation coefficient (PCC) for each iteration, given by equation 6.

$$PCC = \frac{\sum_{i=1}^n ((x_i - \bar{x})(y_i - \bar{y}))}{\sqrt{\sum_{i=1}^n (x_i - \bar{x})^2 \sum_{i=1}^n (y_i - \bar{y})^2}} \quad (6)$$

Where  $\bar{x}$  and  $\bar{y}$  denote the mean intensities and  $x_i$  and  $y_i$  denote the intensity value of the  $i^{\text{th}}$  pixel of the referenced and the to be compared image respectively. The iteration with the highest PCC score of each protocol is taken as the basis for further analysis.

Images were reconstructed using  $4 \times 4 \times 4 \text{ mm}^3$  voxels. The values of the reconstructed image are not directly comparable to the original emission map, because no quantifiable reconstruction method was used. The reconstructed image is scaled to the original image by setting the 99<sup>th</sup> percentile of the cumulative histogram of both images equal to one another. This ensures that any outliers are not taken into account.

The reconstructed images were compared with the emission map and the results for different protocols to each other. The comparison is done by means of calculating the  $\gamma$ -index, a method for comparing dose distributions developed by Low et al[15]. Furthermore, we use the structural similarity-Index (SSIM), developed by Wang et al[16] to make a comparison of structural integrity of the image.

#### 2.4.1 The gamma-index

The  $\gamma$ -index gives a quantitative estimation of the general agreement between two images. It is a method especially developed by Low et al[15] to compare emission-maps. When comparing two images using the  $\gamma$ -index, one image is considered to have perfect quality ( $D_r(r)$ ), the so-called reference image, while the other is the image to be compared with the reference image. ( $D_c(r)$ ) The  $\gamma$ -index compares the images voxel-by-voxel based on two parameters. An emission activity difference parameter ( $D_M$ ) is set to be the percentage that the compared image is allowed to deviate from the reference image. This enables the  $\gamma$ -index to compare emission-maps that deviate in intensity. Furthermore, a distance to agreement (DTA),  $d_m$ , parameter is set that governs the maximum distance the voxel position can deviate from the original. This allows the  $\gamma$ -index to compare images where the voxels have shifted compared to the original. For a reference point at  $r_r$  with an emission activity of  $D_r$  the surface of the ellipsoid that defines these acceptance criteria can be written as:

$$1 = \sqrt{\frac{\Delta r^2}{\Delta d_M^2} + \frac{\Delta D^2}{\Delta D_M^2}} \quad (7)$$

where  $\Delta r = |r_r - r_c|$  is the distance between the compared points and  $\Delta D = D_c(r_c) - D_r(r_r)$  is the emission activity difference in value of the points being compared. For the gamma-index to pass, it needs to have at least one point ( $r_c, D_c$ ) in the ellipsoid of acceptance, i.e.[17]:

$$\Gamma_r(r_c, D_c) \equiv \sqrt{\frac{\Delta r^2}{\Delta d_M^2} + \frac{\Delta D^2}{\Delta D_M^2}} \leq 1 \quad (8)$$

The  $\gamma$ -index returns a pixel map of the original size of the compared images where the voxel values are set to be the minimum distance between the compared points i.e.:

$$\begin{aligned} \gamma \leq 1 & \quad \text{The criterion passes} \\ \gamma > 1 & \quad \text{The criterion fails} \end{aligned} \quad (9)$$

A schematic representation by D.A. Low (2010)[18] of the  $\gamma$ -index can be seen in figure 7

#### 2.4.1.1 Interpretation

The  $\gamma$ -index returns the minimum distance between the referenced point and the line intersecting the unit circle. However, this is in an unusual space, as it contains voxel value and distance information as axes. The unit circle has been normalized to the DTA and emission activity difference criteria in  $y$  and  $x$  respectively. The evaluated distribution can be represented in this normalized space as has been in figure 7, returning a line, sheet or hypersheet for one, two and three dimensions respectively. A distance of 1 or lower corresponds to a point within the unit circle and thus a point that is within the criterion, as seen in figure 7a). A minimum distance of greater than 1 does not result in an intersection with the unit circle and thus results in a fail of the gamma-index, as seen in figure 7b) However, the value of the gamma-index contains information by how much the criterion passes or fails. A value of  $\gamma = 1.01$  fails, but only by 1% and value of  $\gamma = 2$  fails by a factor of 2 of the DTA or dose difference criteria.

#### 2.4.2 The SSIM-index

A second method of comparison is made with the SSIM-index. The SSIM-index gives a quantitative estimation of perceived quality. The SSIM has been developed with the human Visual system (HVS) in mind taking into account three components, the luminance,  $l(x, y)$ , the contrast,  $c(x, y)$ , and the structure  $s(x, y)$ . The SSIM-index takes on the form of:

$$S(x, y) = f(l(x, y)^\alpha, c(x, y)^\beta, s(x, y)^\gamma) \quad (10)$$

Where  $\alpha$ ,  $\beta$  and  $\gamma$  are parameters to weigh the importance of each component. For the SSIM index to give a quantitative estimation of image quality it has to adhere to three conditions:

1. Symmetry:  $S(x, y) = S(y, x)$ .
2. Boundedness:  $S(x, y) \leq 1$
3. Unique maximum  $S(x, y) = 1$  if and only if  $x = y$

The luminance component,  $l(x, y)$ , is defined as:

$$l(x, y) = \frac{2\mu_x\mu_y + C_1}{\mu_x^2 + \mu_y^2 + C_1} \quad (11)$$

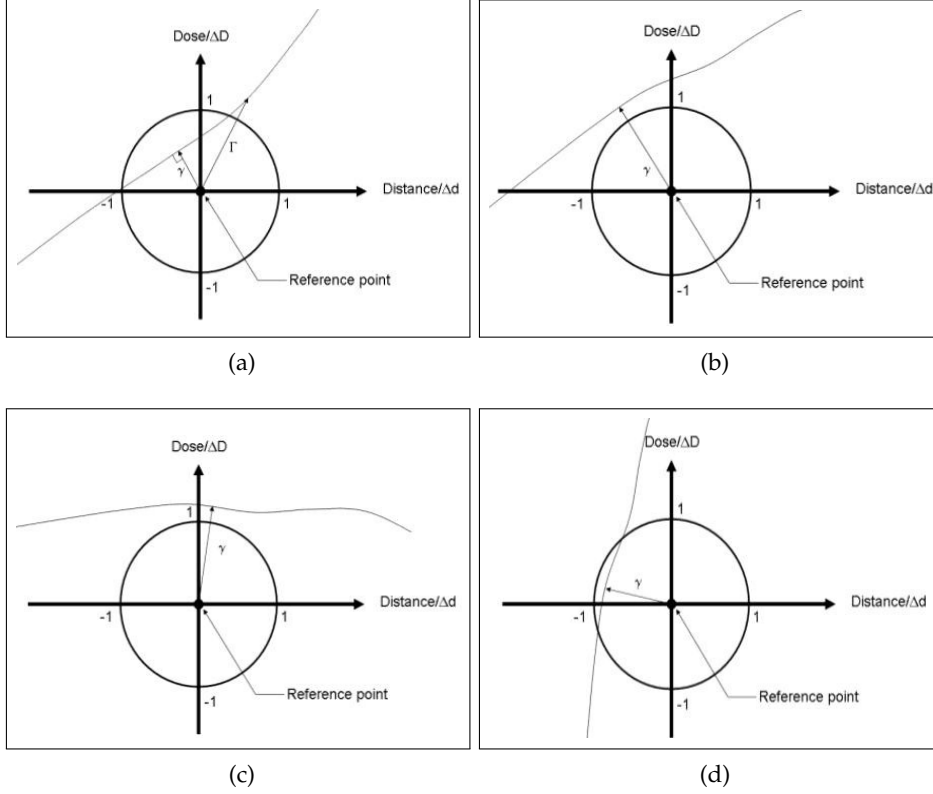


Figure 7: A schematic representation of the  $\gamma$ -index by D.A. Low (2010)[18].  
 (a) The  $\gamma$ -index passes, since the line intersects the unit circle that is defined from the DTA and dose difference criteria. (b) A case where the  $\gamma$ -index fails. (c) A representation of shallow dose-gradient. (d) A representation of a steep dose-gradient.

where  $C_1$  is a constant to counter the instability that arises when  $\mu_x^2 + \mu_y^2$  is very close to zero.  $C_1 = (K_1/L)^2$  where  $L$  is the dynamic range of pixel values and  $K_1$  is a small constant.  $\mu_{x,y}$  are the mean intensities of the image,  $\mu_x = \frac{1}{N} \sum_{i=1}^N x_i$ ,  $\mu_y = \frac{1}{N} \sum_{i=1}^N y_i$ .

The contrast component,  $c(x, y)$ , is defined as;

$$c(x, y) = \frac{2\sigma_x\sigma_y + C_2}{\sigma_x^2 + \sigma_y^2 + C_2} \quad (12)$$

where  $C_2 = (K_2L)^2$  and  $K_2 \ll 1$ .  $\sigma$  is the standard deviation as an estimation of the image contrast, given by:

$$\sigma_x = \left( \frac{1}{N-1} \sum_{i=1}^N (x_i - \mu_x)^2 \right)^{\frac{1}{2}}, \quad \sigma_y = \left( \frac{1}{N-1} \sum_{i=1}^N (y_i - \mu_y)^2 \right)^{\frac{1}{2}}$$

The structural component,  $s(x, y)$ , is defined as;

$$s(x, y) = \frac{\sigma_{xy} + C_3}{\sigma_x\sigma_y + C_3} \quad (13)$$

Where  $C_3 \ll 1$  and chosen to be  $C_3 = C_2/2$ . When the three components, equations 11, 12 and 13 are substituted into equation 10 with an equal weighting of all three components, i.e.  $\alpha = \beta = \gamma = 1$ , we get:

$$\text{SSIM}(x, y) = \frac{(2\mu_x\mu_y + C_1)(2\sigma_{xy} + C_2)}{(\mu_x^2 + \mu_y^2 + C_1)(\sigma_x^2 + \sigma_y^2 + C_2)} \quad (14)$$

The SSIM-index returns a pixel map with the same dimensions as the compared images where every voxel takes on a value between -1 and 1, where a value of 1 can only be achieved when both images are identical.

#### 2.4.2.1 Interpretation

The SSIM-index gives a quantitative estimation of perceived quality. A mean score of the SSIM (*MSSIM*) can be assigned to the whole 3D volume or per image slice where the mean is simply the voxel average value. Since the method is based on the *HVS*, the correlation between SSIM-score and image fidelity is also based on the *HVS*. A mean opinion score has been assigned by Wang et al. (2004) [16] to the *MSSIM* score by evaluating images with said *MSSIM* to the original image.

## RESULTS

A first indication of the best protocol is the number of counts acquired by each protocol, as higher counting statistics lead to a better image. The total number of coincidences of each protocol can be seen in table 4.

Table 4: Number of Coincidences per protocol

Protocol	Coincidences
Protocol 1	4930183
Protocol 2	2926505
Protocol 3	3513713

The second indication in determining the best protocol can be taken from the Pearson Correlation Coefficient (PCC) of the reconstructed images. Which are obtained by comparing the reconstructed image with the emission-map. The PCC score for each iteration can be seen in figure 8. The iteration with the highest PCC is taken as basis for subsequent analysis.

The correlation for Protocol 1 is the strongest. However, the other protocols achieve a similar score meaning that the dual head panels achieve a similar level of image fidelity as the full-ring scanner. Protocol 3 performs better than protocol 2.

The reconstructed images can be seen in figure 9(j), (k), (l) for the transverse view and 10(j), (k), (l) for the sagittal view. At first glance the images from all three protocols give a similar level of image fidelity. All protocols manage to reproduce the general structure of the emission map, as well as the location of high emission activity and regions of lower activity. A quantifiable score of the image fidelity is given by the MSSIM score. The MSSIM values for the 3D volume and local values are found in table 5. Protocol 1 scores the highest, retaining structural information through more counting statistics and a better tomographic coverage. The in-beam protocols show that higher counting statistics are important, since protocol 3 achieves higher scores than protocol 2. Locally, the SSIM-map shows a region of low values to the sides of the head. Furthermore, within the local variances of the SSIM-index, as can be seen in figure 9(g), (h), (i) and 10(g), (h), (i), the highest scores are achieved at the front of the head, reaching scores as high as one, meaning a perfect overlap of the local structure. The dissimilarities arise due to limited angle artifacts, blurring the images and making them less precise when compared to an in-room reconstructed image which does not possess such artifacts.

An overall pass percentage can be defined as the number of pixels of the gamma map with values less than or equal to 1 divided by the

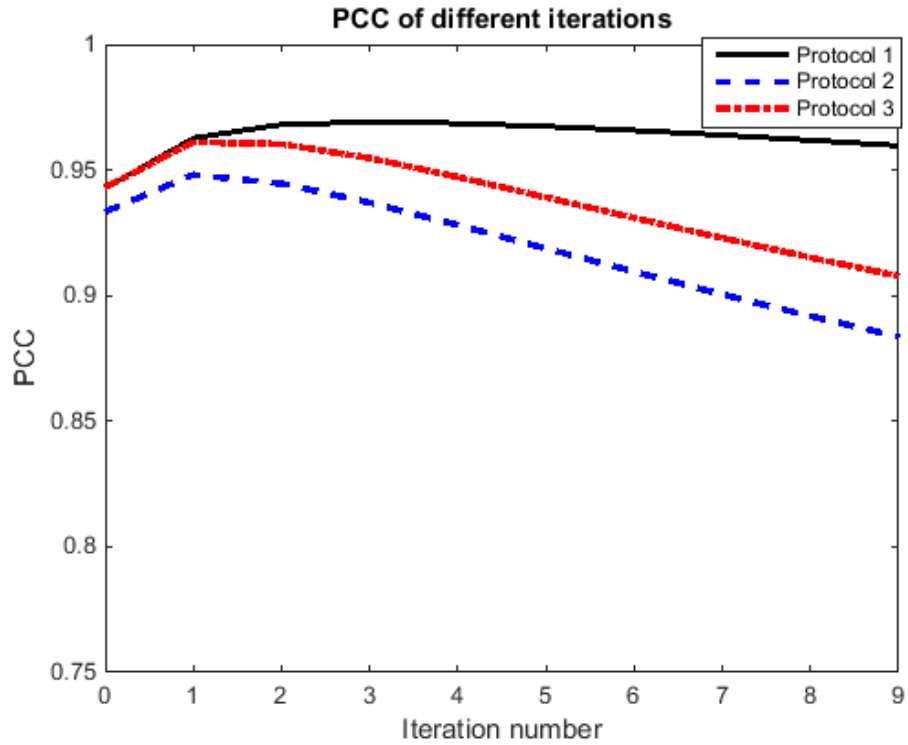


Figure 8: PCC score of the three protocols over different iterations of image reconstruction

total number of pixels present in the 3D volume. The pass percentages of the  $\gamma$ -index are found in table 5, for the whole 3D volume (global) as well as locally for the transverse slices shown in figure 9 and the sagittal slices as shown in figure 10. The highest pass percentages and lowest mean gamma scores are achieved with protocol 1, globally as well as locally. Protocol 2 and 3 achieve lower percentages and higher mean gamma values, meaning that the overall correspondence of the emission map deteriorates for in-beam scanning. Although protocol 2 and 3 achieve similar scores, protocol 3 scores better than protocol 2 on every index, globally as well as locally. Looking at the local gamma map, see figure 9(j), (k), (l) and figure 10(j), (k), (l), one can see that the pixels that pass (indicated from dark red to black) are located throughout the head with protocol 1 containing the most gamma values less than or equal to 1. For protocol 2 and 3, regions of disagreement can be found at the outline of the head, due to limited angle artifacts.

### 3.1 DISCUSSION

Maximum values of  $\gamma = 4$  were calculated at the center of the phantom in all three protocols, this is due to an air-filled cavity inside the patient where almost no emission takes place, resulting in a *cold spot*. This cold spot is most apparent in the sagittal view (figure 10(j), (k), (l)) and has a diameter of roughly 1 cm. Cold spot scanning is difficult due to spillover effects. For cold spots with an diameter of less than two times the scanner resolution spillover occurs, resulting in al-

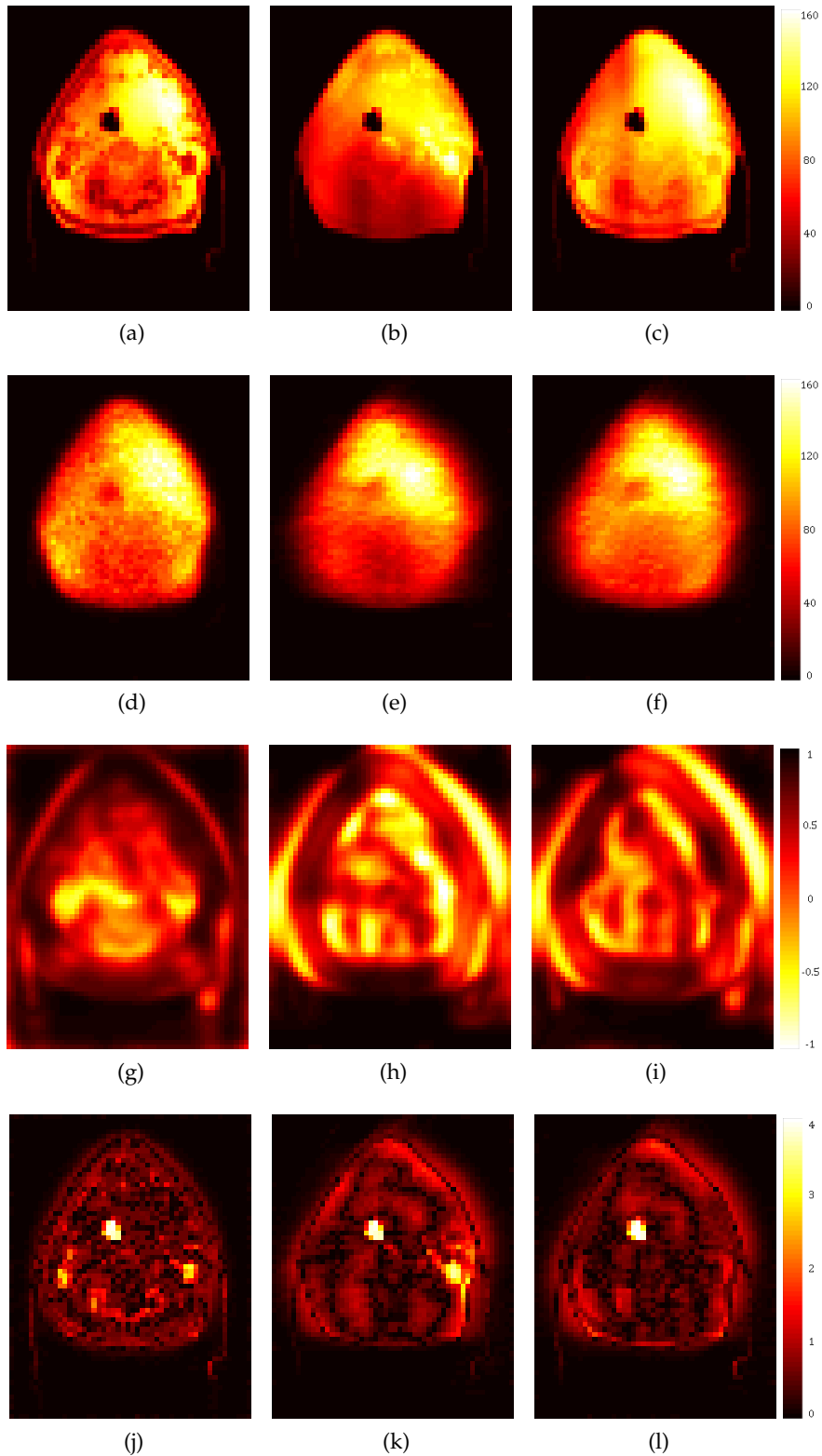


Figure 9: Transverse slices of the patient with different reconstructed images of different protocols taken halfway through the transverse orientation. The columns depict protocol 1, 2 and 3 respectively. the rows denote the emission map ((a), (b), (c)), the reconstructed image scaled with at the 99<sup>th</sup> percentile ((d), (e), (f)), the SSIM-map ((g), (h), (i)), and the Gamma-map with DTA=8mm and a dose difference of 10% ((j), (k), (l))).

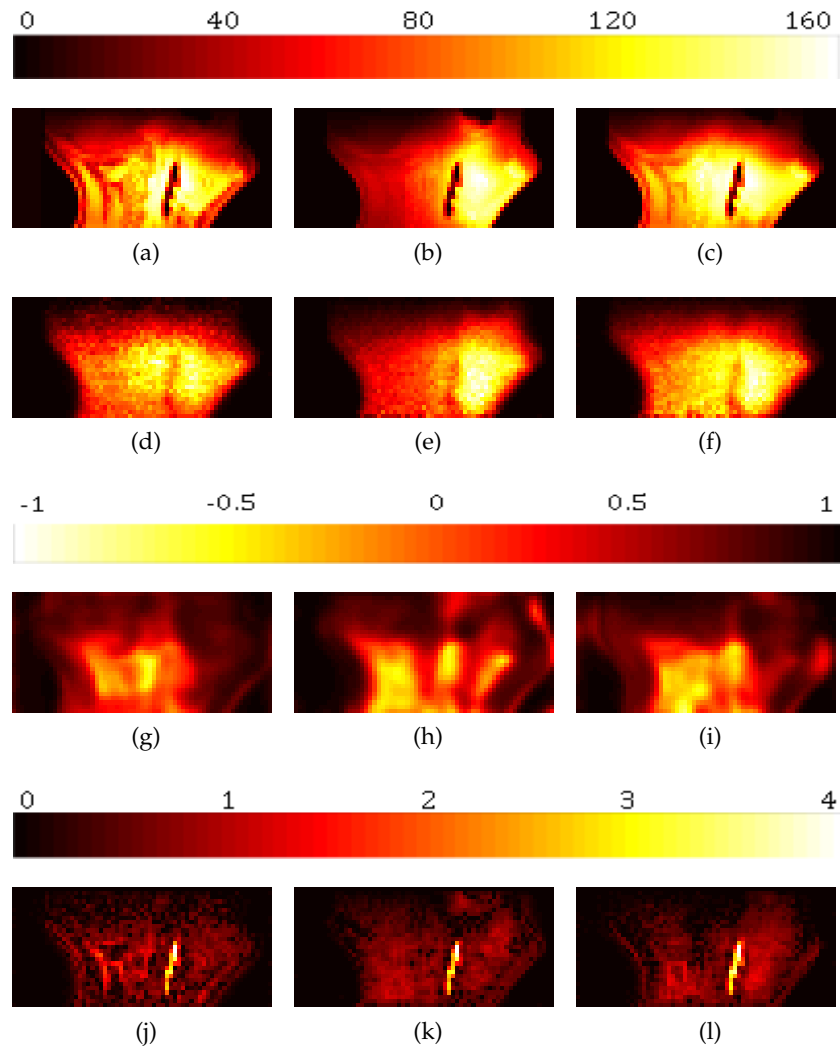


Figure 10: Sagittal slices of the patient with different reconstructed images of different protocols taken halfway through the sagittal orientation. The columns depict protocol 1, 2 and 3 respectively. the rows denote the emission map ((a), (b), (c)), the reconstructed image scaled with at the 99<sup>th</sup> percentile ((d), (e), (f)), the SSIM-map ((g), (h), (i)), and the Gamma-map with DTA=8mm and a dose difference of 10% ((j), (k), (l)).

	Protocol 1	Protocol 2	Protocol 3
PCC	0.9691	0.9481	0.9611
<b>Global</b>			
Percentage Pass $\gamma$ -index	98.49%	96.23%	96.90%
Mean $\gamma$ -index	0.2065	0.2497	0.2480
Mean SSIM	0.8448	0.7627	0.7864
<b>Transverse</b>			
Percentage Pass $\gamma$ -index	96.92%	93.33%	93.62%
Mean $\gamma$ -index	0.2623	0.3408	0.3282
Mean SSIM	0.8033	0.6826	0.7075
<b>Sagittal</b>			
Percentage Pass $\gamma$ -index	96.88%	96.77%	94.47%
Mean $\gamma$ -index	0.2988	0.3510	0.3407
Mean SSIM	0.8030	0.7740	0.7924

Table 5: Scores of different image comparison methods. Global refers to the whole 3D image whereas Transverse refers to the transverse slice midway the region of interest (ROI) as seen in figure 9 and Sagittal refers to the sagittal slice midway the ROI as seen in figure 10

location of activity in surrounding voxels. This results in an increased measured activity in the cavity.

The dual head panels have limited placement possibilities. Furthermore, the whole emission-map does not fit within the field of view, due to obstruction by the patient's shoulders of the dual-head panels (see figure 5b). *Head-and-neck* cases are less susceptible to this loss of field of view since the tumor is contained within the head and neck region. Therefore tumor location is an important consideration for dual-head scanning.

However, for cases where the tumor is located solely in the neck, the dual-head panels are able to reproduce images of similar quality as a full-ring scanner. Furthermore, the dual-head panels allow for scanning between treatment fields, enabling the ability to verify dose deposition during the treatment.

Further improvements on ToF-PET will reduce the limited angle artifacts seen in the reconstructed images. These artifacts are a major component in the disagreement of the  $\gamma$ -index as well as the SSIM. Therefore, the improvements on ToF are most beneficial for dual-head scanners.

In-room delay has been set at 60 seconds, however longer delay times of up to 204s have been simulated in other studies [5][19]. Longer delay times result in less coincidences thus decreasing the image fidelity of the full-ring scanner.

Biological washout is not taken into account and will result in lower counting statistics after a period of delay [20]. This effect would worsen the coincidence numbers of in-room PET scanning, emphasizing the advantage of the minimal delay of dual-head panels.

## CONCLUSIONS

---

Reconstructed Positron Emission Tomography (PET) images of a full-ring and dual-head scanner have been compared to simulated emission-maps of a *head-and-neck* patient taking into account different scanning protocols. These images have been compared using the  $\gamma$ -index, Structural Similarity Index (SSIM) and Pearson Correlation Coefficient (PCC) to determine an optimal protocol for proton therapy dose delivery verification.

Full-ring PET remains the gold standard, with higher sensitivity, and achieving the highest  $\gamma$ -index, SSIM-index and PCC scores both globally and locally.

PET verification with the dual-head scanner is especially applicable to *head-and-neck* cases where the panels can be placed as close as possible to the patient. Dual-head scanners allow for scanning between irradiation fields, allowing for intermediate checking on dose deposition position. Such a scanning protocol would be at the expense of counting statistics, which is a main factor for increased image fidelity as demonstrated by the consistently higher scoring of the dual-head protocol with the highest sensitivity (protocol 3) as opposed to the dual-head protocol with less sensitivity (protocol 2).

Limited-angle artifacts present in dual-head protocols are the main factor of the lower image fidelity and can be mitigated by an improvement of Time of Flight-PET (ToF-PET). Such an improvement could significantly improve the image fidelity of dual-head scanners. Furthermore, taking into account the rather short delay time between treatment and scanning for the in-room PET simulation and the lack of a model for biological washout, which both will degrade the quality of in-room PET, may make dual-head scanning an optimal protocol for *head-and-neck* cases.

Dual-head PET may be a cost effective alternative for full-ring in-room PET, attaining image fidelity on the same level as full-ring PET.



## BIBLIOGRAPHY

---

- [1] Paganetti H. 'Range uncertainties in proton therapy and the role of Monte Carlo simulations'. In: *Physics in Medicine and Biology* 57.11 (2012). DOI: [10.1088/0031-9155/57/11/R99](https://doi.org/10.1088/0031-9155/57/11/R99).
- [2] Ainsley C and Yeager C. 'Practical considerations in the calibration of CT scanners for proton therapy'. In: *Journal of Applied Clinical Medical Physics* 15.3 (2014). DOI: [10.1120/jacmp.v15i3.4721](https://doi.org/10.1120/jacmp.v15i3.4721).
- [3] Roeske JC et al. 'Evaluation of changes in the size and location of the prostate, seminal vesicles, bladder, and rectum during a course of external beam radiation therapy'. In: *International Journal of Radiation Oncology\*Biophysics* 33.5 (1995), pp. 1321–329. DOI: [10.1016/0360-3016\(95\)00225-1](https://doi.org/10.1016/0360-3016(95)00225-1).
- [4] Erridge SC et al. 'Portal imaging to assess set-up errors, tumor motion and tumor shrinkage during conformal radiotherapy of non-small cell lung cancer'. In: *Radiotherapy and Oncology* 66.1 (2003), pp. 75–85. DOI: [10.1016/S0167-8140\(02\)00287-6](https://doi.org/10.1016/S0167-8140(02)00287-6).
- [5] Zhu X and El Fakhri G. 'Proton Therapy Verification with PET Imaging'. In: *Theranostics* 3.10 (2013), pp. 731–40. DOI: [10.7150/thno.5162](https://doi.org/10.7150/thno.5162).
- [6] Sportelli G, Belcaril N, Camarlinghi N, Cirrone GAP, Cuttone G, Ferrettil S and Kraan. A. 'First full-beam PET acquisitions in proton therapy with a modular dual-head dedicated system'. In: *Phys Med Biol* 59.1 (2014). DOI: [10.1088/0031-9155/59/1/43](https://doi.org/10.1088/0031-9155/59/1/43).
- [7] Enghardt W, Crespo P, Fiedler F, Hinz R, Parodi K et al. 'Charged hadron tumour therapy monitoring by means of PET.' In: *Nucl Instrum Methods* 525 (2004), pp. 284–88. DOI: [10.1016/j.nima.2004.03.128](https://doi.org/10.1016/j.nima.2004.03.128).
- [8] Segré E, Bethe H, Ashking J, Bainbridge K, Ramsey N and Staub H. *Experimental Nuclear Physics*. Vol. 1. John Wiley & Sons Inc., 1953, p. 223.
- [9] Parodi K et al. *Proton Therapy Physics*. Medical Physics and Biomedical Engineering. CRC Press, 2011. Chap. In Vivo Dose Verification. ISBN: 9781439836446.
- [10] Saha GB. *Basics of PET Imaging: Physics, Chemistry, and Regulations*. Springer International Publishing, 2015. ISBN: 9783319164236.
- [11] Vishwanath PS and Badiger NM. 'Effective atomic numbers of some tissue substitutes by different methods: A comparative study'. In: *Med Phys* 39.1 (2014), pp. 24–31. DOI: [10.4103/0971-6203.125489](https://doi.org/10.4103/0971-6203.125489).

- [12] *Truly digital PET imaging*. Brochure. Phillips Vereos PET/CT. 2015. URL: [http://incenter.medical.philips.com/doclib/enc/11230947/Digital\\_PET\\_Tech\\_Overview\\_rev\\_Jul\\_2015\\_\(1\).pdf%3ffunc%3ddoc.Fetch%26nodeid%3d11230947](http://incenter.medical.philips.com/doclib/enc/11230947/Digital_PET_Tech_Overview_rev_Jul_2015_(1).pdf%3ffunc%3ddoc.Fetch%26nodeid%3d11230947).
- [13] David Brasse, Paul E. Kinahan, Carole Lartizien, Claude Comtat, Mike Casey and Christian Michel. 'Correction Methods for Random Coincidences in Fully 3D Whole-Body PET: Impact on Data and Image Quality'. In: *Journal of Nuclear Medicine* 46.5 (2005), pp. 859–67.
- [14] Washington CM and Leaver DT. *Principles and Practice of Radiation Therapy*. 4th. 525. Elsevier Health Sciences, 2015.
- [15] Low DA, Harms WB, Muttic S and Purdy JA. 'A technique for the quantitative evaluation of dose distributions'. In: *Phys Med* 51.5 (1998), pp. 656–61. DOI: [10.1118/1.598248](https://doi.org/10.1118/1.598248).
- [16] Wang Z et al. 'Image Quality Assessment: From Error Measurement to Structural Similarity'. In: *IEEE Transactions on Image Processing* 13.1 (2004), pp. 600–12. DOI: [10.1109/TIP.2003.819861](https://doi.org/10.1109/TIP.2003.819861).
- [17] Depuydt T et al. 'A quantitative evaluation of IMRT dose distributions: refinement and clinical assessment of the gamma evaluation'. In: *Radiotherapy and Oncology* 62.3 (2002), pp. 309–19. DOI: [10.1016/S0167-8140\(01\)00497-2](https://doi.org/10.1016/S0167-8140(01)00497-2).
- [18] Low DA. 'Gamma Dose Distribution Evaluation Tool'. In: *Journal of Physics: Conference Series* 250.1 (2010), p. 012071. DOI: [1742-6596/250/i=1/a=012071](https://doi.org/10.1088/1742-6596/250/i=1/a=012071).
- [19] Zhu X, España S, Daartz J, Liebsch N, Ouyang J, Paganetti H, Bortfeld TR and Fakhri G. 'Monitoring proton radiation therapy with in-room PET imaging'. In: *Physics in Medicine and Biology* 56.13 (2011), p. 4041. DOI: [0031-9155/56/i=13/a=019](https://doi.org/10.1088/0031-9155/56/i=13/a=019).
- [20] Martínez-Rovira I, C. Jouvie and Jan S. 'Technical Note: Implementation of biological washout processes within gate/geant4—A Monte Carlo study in the case of carbon therapy treatments'. In: *Medical Physics* 42.4 (2015), pp. 1773–1778. DOI: <http://dx.doi.org/10.1118/1.4914449>.